ORIGINAL PAPER

A height-resolving tropical cyclone boundary layer model with vertical advection process

Jian Yang[1] · Yu Chen[1] · Hua Zhou[1] · Zhongdong Duan[1]

Abstract

The height-resolving model is thought to be an optimal scheme for modeling the tropical cyclone (TC) wind fields in the boundary layer because it explicitly depicts the wind structures in that layer as TC evolves over time. However, the vertical advection process which exists in TCs has not been well considered in previously proposed parametric TC models. Neglecting this process may cause deviations of the simulated wind field structure in the boundary layer. Herein, a height-resolving boundary layer wind field model incorporating both the vertical advection and vertical diffusion processes is proposed and a semi-analytical solution to the governing equations is developed. The adequacy of this model is evaluated by comparing with the Weather Research and Forecasting model simulations, the Hurricane Research Division's H*Wind snapshots, GPS dropsonde datasets and ground measurements of several TC events. Results show that the proposed model with vertical advection can reasonably produce the wind fields of TCs, and its advantage lies in the production of a more realistic three-dimensional wind structure in the boundary layer.

1 Introduction

Tropical cyclone (TC) is a vortex storm with central low-pressure and well-organized convection. A reasonable wind field model of TC boundary layer is critical to explore the wind effects on building structures and TC hazard analyses. Most parametric TC wind models estimate the surface wind by the gradient wind multiplying a wind reduction factor, varying from 0.65 to 0.95 in different studies (Vickery et al. 2009a), e.g., a wind reduction factor of 0.865 was used in Batts et al. (1980), while Sparks and Huang (2001) recommended 0.65 and 0.62 under ocean and open coastal conditions, respectively. Although the wind reduction factor has been widely used in TC hazard analyses (Chen and Duan 2018; Powell et al. 2005), it does not capture the key features of TC wind fields. For instance, Franklin et al. (2003) discovered

✉ Zhongdong Duan
 duanzd@hit.edu.cn

1 School of Civil and Environmental Engineering, Harbin Institute of Technology, Shenzhen 518055, Guangdong, China

the jet feature of TC by studying the dropsonde-derived mean vertical wind profiles (wind speed profiles along height). They pointed out that the peak wind in the eyewall at the height of 500 m was nearly 20% larger than that at the height of 700 hPa. Schwendike and Kepert (2008) discussed the boundary layer structures of two hurricanes and found that the boundary layer height decreases with the distance from the TC center decreases.

In order to accurately simulate the TC wind field, many TC boundary layer models have been proposed, which fall into two categories, namely the depth-averaged (also known as slab) models (Chow 1971; Li and Hong 2015; Shapiro 1983; Thompson and Cardone 1996; Xiao et al. 2011) and the height-resolving models (Kepert 2001; Meng et al. 1995; Snaiki and Wu 2017a). As described by Thompson and Cardone (1996), their slab model estimated the near-surface wind by using a parametric relationship between the vertically averaged wind speed and the friction velocity. This model has been widely used in storm surge simulations and wind hazard assessments (Hong et al. 2016; Vickery et al. 2009c). However, there are several defects in the slab model, such as the assumptions of vertically averaged wind speed and constant boundary layer height (Kepert 2010a, 2010b).

The height-resolving model captures the physical processes that vary with height and helps to reveal the TCs' horizontal and vertical structures. Meng et al. (1995) presumed that the TC wind speed in the boundary layer could be decomposed into the gradient wind speed and the friction caused wind speed, and then, linearized solutions were obtained by applying the perturbation analysis. Later, Kepert (2001) improved the height-resolving model by simplifying the vertical diffusion, linearizing the horizontal advection and neglecting the vertical advection. Recently, these models have been further developed by several scholars for engineering applications (Fang et al. 2018; Li et al. 2020; Snaiki and Wu 2017a, 2017b). However, as discussed by Kepert and Wang (2001), a critical problem of the current height-resolving model is that the simulated supergradient wind is weaker than the observation because it disregards the vertical advection to facilitate model solution. Proper inclusion of the vertical advection will not only improve TC wind field simulation, but also help predict the TC-driven rainfall, which is strongly related to the vertical wind component of TC (Langousis and Veneziano 2009).

In this paper, the main objectives include: 1) to develop a height-resolving TC model with the horizontal advection, vertical advection and vertical diffusion; 2) to study the effects of vertical advection on TC wind fields; 3) to evaluate the adequacy of our model in simulating the TC horizontal and vertical wind components. This height-resolving model is similar to the one considered by Kepert (2001), but the vertical advection process is considered in this study, and the continuity equation is added to solve the vertical wind component. In addition, this paper adopts a fast method of solving the TC wind fields based on a combination of the analytical and finite difference methods, which differs from Kepert (2001). The organization of the paper is as follows. In Sect. 2, the formulation and solution procedures of the TC model are presented. In Sect. 3, several cases are conducted to investigate the TC structure and super-gradient phenomena. In Sect. 4, the model is verified by comparing the Weather Research and Forecasting (WRF) model simulations, the Hurricane Research Division's H*Wind snapshots, GPS dropsonde datasets and ground measurements of several TC events. In the last section, major findings of this study are summarized.

2 Model formulation and its solution procedures

2.1 Governing equations

The kinetic equation for air parcel (Holton 2007; Thompson and Cardone 1996) in the coordinate system fixed to the earth can be expressed as

$$\frac{d\hat{\mathbf{V}}}{dt} + f \cdot k \times \hat{\mathbf{V}} = -\frac{1}{\rho}\nabla\hat{\mathbf{P}} + F \tag{1}$$

where $d/dt = \partial/\partial t + \hat{\mathbf{V}} \cdot \nabla$; $\hat{\mathbf{V}}$ is the velocity of air parcel; f is the Coriolis parameter; k is the unit vector in vertical direction; $\rho = 1.2$ kg/m^3 is the mean air density; $\hat{\mathbf{P}}$ is the atmospheric pressure, F is the frictional force.

$\hat{\mathbf{V}}$ can be expressed as the sum of the wind velocity $\mathbf{V}$ relative to TC center and the TC moving velocity $\mathbf{V}_c$; $\hat{\mathbf{P}}$ is assumed to be the sum of the axisymmetric TC pressure field p and the large-scale pressure field p_L, which has $-\nabla p_L/\rho = f \cdot k \times \mathbf{V}_c$. Then, Eq. (1) can be rewritten as

$$\frac{\partial \mathbf{V}}{\partial t} + \mathbf{V}_c \cdot \nabla\mathbf{V} + \mathbf{V} \cdot \nabla\mathbf{V} + f \cdot k \times \mathbf{V} = -\frac{1}{\rho}\nabla p + F \tag{2}$$

Replacing $\mathbf{V}$ by $\mathbf{v}_g + \mathbf{v}'$, where $\mathbf{v}_g$ is the gradient wind; $\mathbf{v}'$ is the friction caused wind (Meng et al. 1995). In order to facilitate the solution of $\mathbf{v}_g$ and $\mathbf{v}'$, Eq. (2) is decomposed into two separate equations as

$$\frac{\partial \mathbf{v}'}{\partial t} + \mathbf{V}_c\nabla\mathbf{v}' + \mathbf{v}_g\nabla\mathbf{v}' + \mathbf{v}'\nabla\mathbf{v}_g + \mathbf{v}'\nabla\mathbf{v}' = -f \cdot k \times \mathbf{v}' + F \tag{3}$$

$$\frac{\partial \mathbf{v}_g}{\partial t} + \mathbf{V}_c\nabla\mathbf{v}_g + \mathbf{v}_g\nabla\mathbf{v}_g = -\frac{1}{\rho}\nabla p - f \cdot k \times \mathbf{v}_g \tag{4}$$

$\partial \mathbf{v}'/\partial t$ in Eq. (3) is significantly smaller than the other terms and it will be ignored in the following discussions (Meng et al. 1995). In the friction-free atmosphere, the gradient wind $\mathbf{v}_g$ is assumed steady, which renders the unsteady term $\partial \mathbf{v}_g/\partial t$ in Eq. (4) to be zero. Compared to $\mathbf{v}_g$, $\mathbf{V}_c$ is much smaller and $\mathbf{V}_c\nabla\mathbf{v}_g$ is also neglected here.

Scale analysis, which has been used and verified by several researchers (Fang et al. 2018; Snaiki and Wu 2017a; Vogl and Smith 2009), is used to simplify Eq. (3). As a result of the scale analysis (see detailed derivations in "Appendix 1"), the following equations are obtained in the cylindrical coordinate system (r, λ, z), as shown in Fig. 1,

$$\frac{v_g}{r}\frac{\partial u'}{\partial \lambda} - \left(\frac{2v_g}{r} + f\right)v' + w'\frac{\partial u'}{\partial z} = K_v\frac{\partial^2 u'}{\partial z^2} \tag{5}$$

$$\frac{v_g}{r}\frac{\partial v'}{\partial \lambda} + \left(\frac{\partial v_g}{\partial r} + \frac{v_g}{r} + f\right)u' + w'\frac{\partial v'}{\partial z} = K_v\frac{\partial^2 v'}{\partial z^2} \tag{6}$$

in which, K_v is the vertical eddy viscosity coefficient; u', v' and w' are the radial, tangential and vertical components of $\mathbf{v}'$, respectively; v_g is the tangential gradient wind component; the radial gradient wind component u_g is small and neglected. Equations (5) and (6)

Fig. 1 Wind components in the cylindrical coordinate system (r, λ, z). φ is the TC moving angle, and $\mathbf{V}_c$ is the TC moving velocity
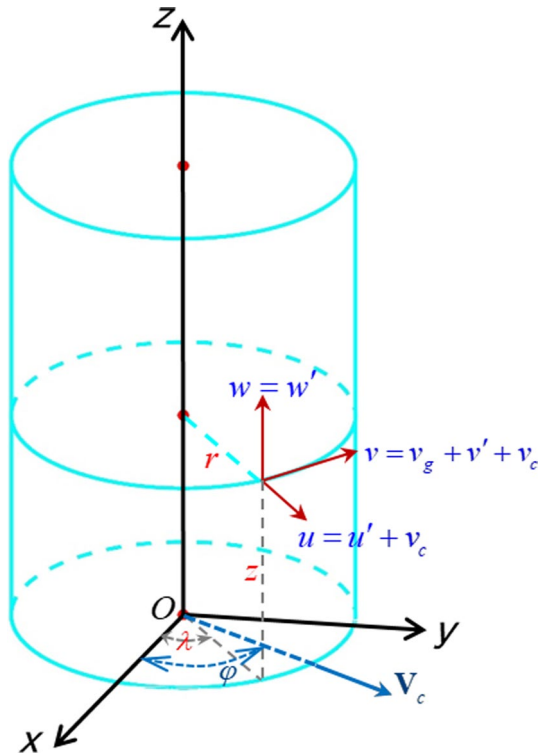
represent the balance among the azimuthal advection, radial advection, vertical advection and vertical diffusion.

Different from existing TC wind field models (Kepert 2001; Meng et al. 1995), the terms of vertical advection $w'\partial/\partial z$ are introduced in Eqs. (5) and (6). The radial and azimuthal flow balance equations of Meng et al. (1995), Kepert (2001) and this proposed model are compared in Table 1. The performance of these three TC models will be compared in the following sections.

In order to solve Eqs. (5) and (6), the continuity equation is introduced. In atmospheric boundary layer, the air density is assumed to be constant and the compressibility of air is ignored. The continuity equation can be expressed as

$$\frac{\partial(ru)}{\partial r} + \frac{\partial v}{\partial \lambda} + \frac{\partial(rw)}{\partial z} = 0 \tag{7}$$

2.2 Boundary conditions

Following Holland (1980), the axisymmetric TC pressure field is presented as

$$p = p_0 + \Delta p \cdot \exp\left[-\left(\frac{R_{max}}{r}\right)^B\right] \tag{8}$$

Table 1 The radial and azimuthal flow balance equations of Meng model, Kepert model and our proposed model

Model	Meng et al. (1995)	Kepert (2001)	Proposed model
Radial flow balance	$-\left(\frac{2v_g}{r}+f\right)v' = K_v \frac{\partial^2 u'}{\partial z^2}$	$\frac{v_g}{r}\frac{\partial u'}{\partial \lambda} - \left(\frac{2v_g}{r}+f\right)v' = K_v \frac{\partial^2 u'}{\partial z^2}$	$\frac{v_g}{r}\frac{\partial u'}{\partial \lambda} - \left(\frac{2v_g}{r}+f\right)v' + w'\frac{\partial u'}{\partial z} = K_v \frac{\partial^2 u'}{\partial z^2}$
Azimuthal flow balance	$\left(\frac{\partial v_g}{\partial r}+\frac{v_g}{r}+f\right)u' = K_v \frac{\partial^2 v'}{\partial z^2}$	$\frac{v_g}{r}\frac{\partial v'}{\partial \lambda} + \left(\frac{\partial v_g}{\partial r}+\frac{v_g}{r}+f\right)u' = K_v \frac{\partial^2 v'}{\partial z^2}$	$\frac{v_g}{r}\frac{\partial v'}{\partial \lambda} + \left(\frac{\partial v_g}{\partial r}+\frac{v_g}{r}+f\right)u' + w'\frac{\partial v'}{\partial z}$ $= K_v \frac{\partial^2 v'}{\partial z^2}$

in which, p_0 is the TC central pressure; Δp is the difference between the TC central pressure (p_0) and the standard atmospheric pressure (1010 hPa is used in this paper); R_{max} is the radius to the maximum wind; B is the pressure profile coefficient. R_{max} and B can be estimated as following (Vickery and Wadhera 2008)

$$R_{\max} = \exp\left(3.015 - 6.291 \times 10^{-5}\Delta p^2 + 0.0337 \cdot lat\right) \tag{9}$$

$$B = 1.833 - 0.326\sqrt{f \cdot R_{\max}} \tag{10}$$

where lat is the latitude of TC center. The tangential gradient wind component v_g in Eqs. (5) and (6) can be solved by Eq. (4) as follows

$$v_g = \frac{-f \cdot r}{2} + \sqrt{\left(\frac{-f \cdot r}{2}\right)^2 + \frac{r}{\rho}\frac{\partial p}{\partial r}} \tag{11}$$

Two assumptions of the bottom boundary conditions are used, i.e., the well-mixed boundary layer and the flux-gradient theory (Holton 2007), which are

$$K_v\left(\frac{\partial u}{\partial z}\right)_s = C_d \cdot \hat{\mathbf{V}} \cdot u \tag{12}$$

$$K_v\left(\frac{\partial v}{\partial z}\right)_s = C_d \cdot \hat{\mathbf{V}} \cdot v \tag{13}$$

where u and v are radial and tangential wind components of $\hat{\mathbf{V}}$, respectively, and $u = u' + u_c$, $v = v_g + v' + v_c$; the resultant wind $\hat{\mathbf{V}} = \sqrt{(u' + u_c)^2 + (v_g + v + v_c)^2}$; C_d is the drag coefficient; u_c and v_c are the radial and tangential components of $\mathbf{V}_c$, respectively, which are given by

$$u_c = \frac{\mathbf{V}_c}{2} \cdot (e^{i\lambda} + e^{-i\lambda}) \tag{14}$$

$$v_c = \frac{\mathbf{V}_c}{2}i \cdot (e^{-i\lambda} - e^{i\lambda}) \tag{15}$$

Thus, Eqs. (12) and (13) become

$$K_v\left(\frac{\partial u'}{\partial z}\right)_s = C_d\sqrt{(u' + u_c)^2 + (v_g + v' + v_c)^2}(u' + u_c) \tag{16}$$

$$K_v\left(\frac{\partial v'}{\partial z}\right)_s = C_d\sqrt{(u' + u_c)^2 + (v_g + v' + v_c)^2}(v_g + v' + v_c) \tag{17}$$

$\mathbf{V}_c$ is reasonably assumed to be much smaller than v_g, and linearization can be made to the terms at the right-hand-side of Eqs. (16) and (17). At the near ground surface ($z \to 0$), Eqs. (16) and (17) are simplified as (Kepert 2001)

$$K_v \left(\frac{\partial u'}{\partial z} \right)_{z \to 0} = C_d v_g [u'(0) + u_c] \tag{18}$$

$$K_v \left(\frac{\partial v'}{\partial z} \right)_{z \to 0} = C_d v_g [v_g + 2v'(0) + 2v_c] \tag{19}$$

For the top boundary conditions, we assume that the simulated wind speed is equal to the gradient wind speed and does not change with height, i.e., $\partial u/\partial z = \partial v/\partial z = 0$.

2.3 Solve for TC boundary layer wind

In order to solve Eqs. (5), (6), and (7) for u', v' and w' by adopting the boundary conditions of Eqs. (18) and (19), new variables are introduced, namely

$$\alpha = \frac{1}{2K_v} \left(f + \frac{2v_g}{r} \right), \beta = \frac{1}{2K_v} \left(f + \frac{v_g}{r} + \frac{\partial v_g}{\partial r} \right), \gamma = \frac{1}{2K_v} \frac{v_g}{r}, \delta = \frac{w'}{2K_v} \tag{20}$$

The variable ω used in Kepert (2001) is employed

$$\omega = \sqrt{\frac{\beta}{\alpha}} u' + v' \cdot i \tag{21}$$

where i is the imaginary symbol. Then, Eqs. (5) and (6) can be rewritten uniformly as

$$2\gamma \frac{\partial \omega}{\partial \lambda} + 2\delta \frac{\partial \omega}{\partial z} + 2i\sqrt{\alpha\beta}\omega - \frac{\partial^2 \omega}{\partial z^2} = 0 \tag{22}$$

It is worth noting that Eq. (22) to be solved in this study is different from Kepert (2001), since the vertical movement of air parcel ($\delta = w'/2K_v$) is considered.

The variable ω in Eq. (22) can be expanded as a Fourier series in azimuth

$$\omega(\lambda, z) = \sum_{k=-\infty}^{+\infty} a_k(z) e^{ik\lambda} \tag{23}$$

in which, $a_k(z)$ is a complex coefficient. Then, the following equation can be derived from Eq. (22) using Eq. (23)

$$\sum_{k=-\infty}^{+\infty} \left[2i\left(\gamma k + \sqrt{\alpha\beta}\right) a_k(z) + 2\delta a_k'(z) - a_k''(z) \right] \cdot e^{ik\lambda} = 0 \tag{24}$$

The solution to the above differential equation can be assumed in the form of

$$a_k(z) = A_k \exp(p_k z) \tag{25}$$

where A_k and p_k are constants to be determined. Then, Eq. (24) is transformed into

$$2i(\gamma k + \sqrt{\alpha\beta}) + 2\delta p_k - p_k^2 = 0 \tag{26}$$

Separating u' and v' from ω in Eq. (21) and plugging them into the boundary conditions of Eqs. (18) and (19) gives

$$\text{Re}\left\{ \sqrt{\frac{\alpha}{\beta}} \sum_{k=-\infty}^{+\infty} \left[A_k \left(\frac{C_d v_g}{K_v} - p_k \right) e^{ik\lambda} \right] + \frac{C_d v_g}{2K_v} \cdot \mathbf{V}_c (e^{i\lambda} + e^{-i\lambda}) \right\} = 0 \tag{27}$$

$$\text{Im}\left\{ \sum_{k=-\infty}^{+\infty} \left[A_k \left(\frac{2C_d v_g}{K_v} - p_k \right) e^{ik\lambda} \right] + \frac{C_d v_g}{K_v} \left[iv_g + \mathbf{V}_c (-e^{i\lambda} + e^{-i\lambda}) \right] \right\} = 0 \tag{28}$$

in which, $\text{Re}[f(x)] = [f^*(x) + f(x)]/2$, $\text{Im}[f(x)] = i[f^*(x) - f(x)]/2$, and $f^*(x)$ is the complex conjugate of $f(x)$. According to Kepert (2001), the terms of $|k| \geq 2$ in Eqs. (27) and (28) are neglected; A_k and p_k can be solved from Eqs. (27) and (28); and the friction caused wind components u' and v' are derived from Eqs. (21) and (23) (detailed derivation is shown in "Appendix 2"). Finally, the horizontal wind components in the boundary layer relative to the earth are

$$u(r, \lambda, z) = u'(r, \lambda, z) + u_c \tag{29}$$

$$v(r, \lambda, z) = v'(r, \lambda, z) + v_g + v_c \tag{30}$$

Here, we define $u_c = \mathbf{V}_c \bullet \cos(\lambda - \varphi)$, $v_c = -\mathbf{V}_c \bullet \sin(\lambda - \varphi)$; φ is the TC moving angle, which is counter-clockwise positive from eastward. The vertical wind component w (w') can be computed from the horizontal winds (u, v) by using continuity equation (Eq. (7))

$$w(r, \lambda, z) = -\frac{1}{r} \left[\int_0^z \frac{\partial(ru)}{\partial r} dz + \int_0^z \frac{\partial v}{\partial \lambda} dz \right] \tag{31}$$

Figure 2 shows the simulation flow chart of the proposed TC model. C_d, K_v, and v_g are predefined parameters. δ is assumed to be 0 in the first iteration, and updated iteratively according to w calculated in the previous step. The TC wind field (u, v, w) is calculated iteratively, and this procedure ends when the resultant velocity (V_2) of the current step is close enough to the velocity (V_1) of previous step. In this study, when $|V_2 - V_1| \leq 0.01$ or the number of iterations $n \geq 100$, the simulation ends and the calculated wind field is output. It should be noted that the drag coefficient C_d and the vertical eddy viscosity coefficient K_v are important factors in TC wind field simulations. Kepert (2012) compared several parameterization schemes for K_v and found that the constant length scale l used in K_v could lead to an unsuitable vertical wind profile. More recently, similar results are concluded by Li et al. (2020) who studied the influences of different parameterization methods of K_v and C_d on the TC boundary layer wind field using the Kepert (2001)'s model. In our study, the vertical eddy viscosity coefficient K_v is still taken as a constant value with $K_v = 50$ m^2/s, which is consistent with Kepert (2001). The drag coefficient C_d is calculated by the following equation (Kepert 2012)

$$C_d = \left[\frac{\kappa}{\log(z_1/z_0)} \right]^2 \tag{32}$$

where z_0 is the surface roughness length; z_1 is the height above the ground surface, we take $z_1 = 1$ m in this study; $\kappa = 0.4$ is von Kärmän's constant.

Fig. 2 Simulation flow chart of
the proposed TC model
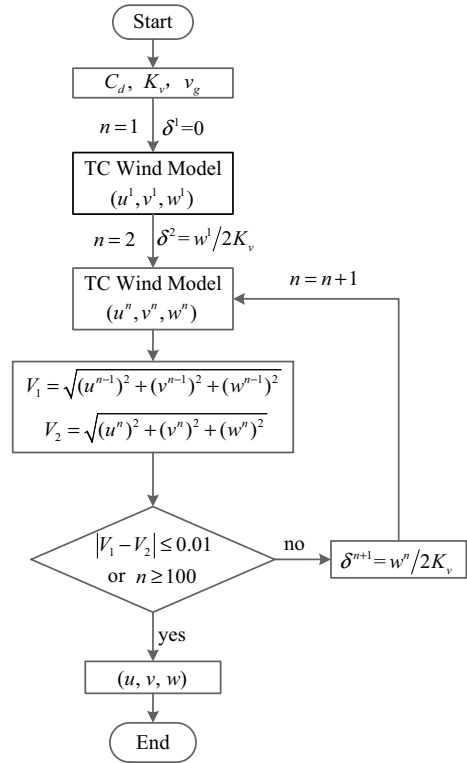
3 Case studies

In this section, we first study the ability of our proposed model to predict the horizontal and vertical sections of TC wind fields. Then, magnitudes of advection and diffusion terms in Eqs. (5) and (6) are investigated, and model comparisons with Meng et al. (1995) (hereafter M95) and Kepert (2001) (hereafter K01) are conducted to study the effects of vertical advection on the prediction of supergradient phenomena.

3.1 Horizontal and vertical sections of wind fields

A TC is assumed to translate northward in the northern hemisphere. The TC pressure field is prescribed by Eq. (8) with $R_{max} = 40$ km, $B = 1.2$, $p_0 = 950$ hPa; the surface roughness length in Eq. (32) is $z_0 = 0.0002$ m, which is assumed to move over the ocean; the Coriolis parameter is $f = 3.8 \times 10^{-5}$ s^{-1} at $lat = 15°$ N; the moving velocity is $\mathbf{V}_c = 5$ m/s. With these parameters, the boundary layer flow of this moving TC is simulated.

The radial wind fields (U), tangential wind fields (V), vertical wind fields (W) and resultant wind fields (T) at heights of 10 m, 100 m, 500 m, 1.0 km and 1.5 km are presented in Fig. 3. The radial wind in TC is mainly affected by the surface friction. As height increases, the friction effect weakens, and thus, the radial wind decreases. This feature is observed in Fig. 3a. Similar to Langousis et al. (2009), the radial wind
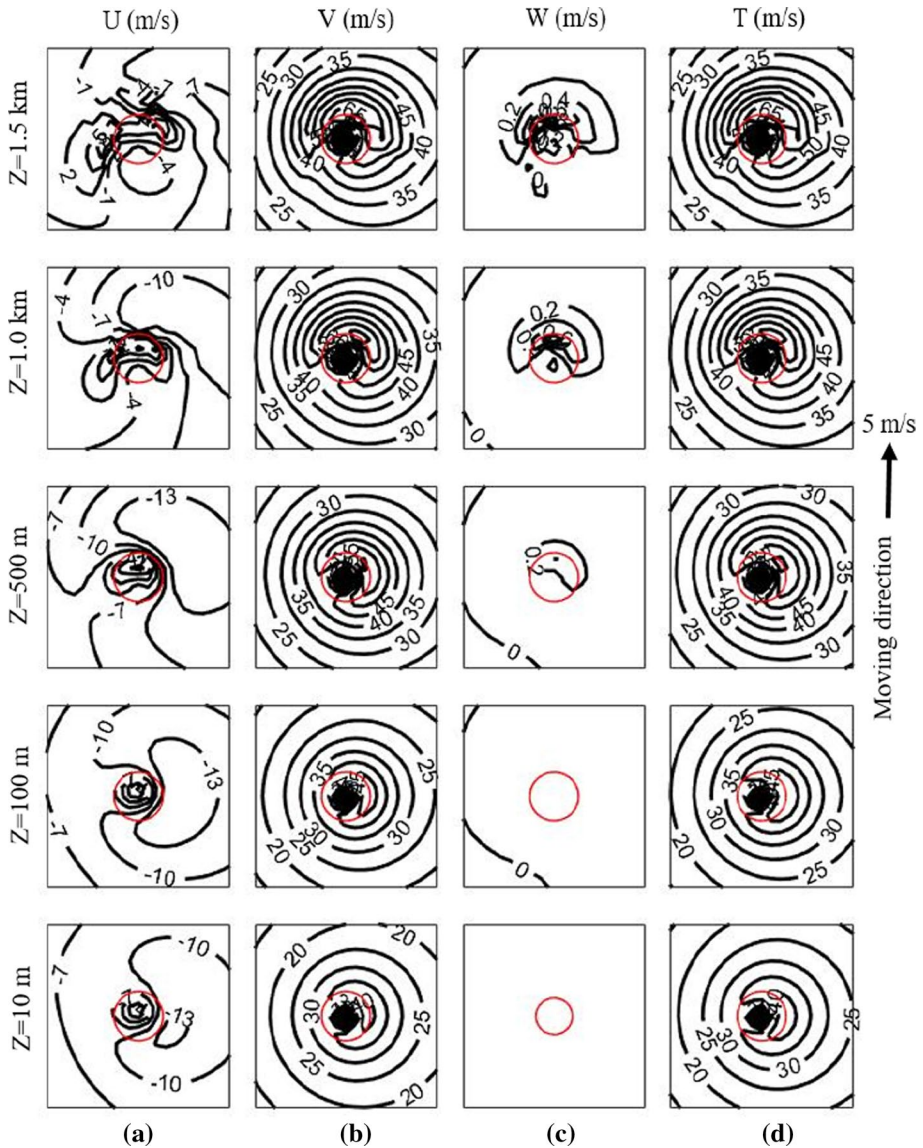
Fig. 3 Boundary layer solution for the (**a**) radial wind fields U, (**b**) tangential wind fields V, (**c**) vertical wind fields W and (**d**) resultant wind fields T at heights of $Z = 10$ m, 100 m, 500 m, 1.0 km and 1.5 km. The red circles are the radius to the maximum wind. The horizontal domain of each graph is 400 km $\times$ 400 km. The TC moves northward with velocity $V_c = 5$ m/s

speed at a lower height ($Z = 100$ m) is larger than that at a higher height ($Z = 1.5$ km). The maximum inflow location rotates counter-clockwise toward the moving direction of TC as the height increases. This will affect the locations of the maximum wind in TC wind field. The magnitude of vertical wind in Fig. 3c increases with height near the

TC eyewall, and it is stronger near the core of TC than in the outer zone. The tangential wind V in Fig. 3b is much larger than U and W, and it controls the structure of TC.

The asymmetric structure of a moving TC shows that the maximum wind speed relative to the earth occurs on the right side of TC moving direction (Shapiro 1983). Li and Hong (2015) found the mean azimuth angle of the maximum wind was 97° from the moving direction located on the right side of TCs by using the Hurricane Research Division's H*Wind snapshots. In this TC case, the simulated maximum wind location is at an angle of about 90° near the ground surface ($Z=10$ m and 100 m) and rotates toward the right front quadrant with increasing height. This may be due to the counter-clockwise rotation of radial inflow shown in Fig. 3a.

Following the case discussed in Fig. 3, the wind speed contours of azimuthally averaged radial, tangential, vertical and resultant wind are studied on a vertical plane through the TC center, as shown in Fig. 4. The depth of inflow layer increases with the increase in distance from the TC eyewall (Fig. 4a), from about 400 m at a radius of 20 km to more than 2000 m at a radius of 180 km. This feature is consistent with observations made by Bell and Montgomery (2008). The maximum inflow is 8.83 m/s at height of 170 m and at radius of 80 km, which is almost twice of R_{max}. Around the R_{max}, our model shows a similar outflow region (Fig. 4a) as illustrated in Kepert's high-order closure vertical diffusion scheme model; however, at outer radius, the outflow region turns to be similar to Kepert's simple mixing-length scheme model (Kepert (2010a), his Figs. 1 and 2). This shows the effect of vertical advection on the distribution of inflow area. Above the inflow layer, the outflow (shaded in Fig. 4a) is relatively weak with values less than 2.5 m/s.

In Fig. 4b, the azimuthally averaged tangential wind speed no longer increases monotonously with height in the vicinity of TC eyewall, and the supergradient phenomenon is revealed. The maximum tangential wind is 42.9 m/s at the radius of 41 km and height of 710 m, which is about 6.6% larger than the gradient wind. The vertical velocity shown in Fig. 4c reaches a peak value of 0.25 m/s at 1400 m near the R_{max}. At large radii (about 230 km), weak descent velocity occurs. By comparing Figs. 4a, c and d, one can find that the supergradient flow reaches its maximum within the inflow area and is strongly enhanced in the vertical ascent flow region and weakened at large radii.

3.2 Magnitudes of the advection and diffusion terms

Each term of the governing equations (Eqs. 5 and 6) is evaluated in this section by using the same TC case described in Fig. 3. Magnitudes of the azimuthally averaged azimuthal advection, radial advection, vertical advection and vertical diffusion at R_{max} are shown in Fig. 5. In this figure, $AAR = v_g/r \cdot \partial u'/\partial \lambda$ represents the azimuthal advection of radial flow; $RAR = -(2v_g/r+f) \cdot v'$ represents the radial advection of radial flow; $VAR = w' \partial u'/\partial z$ represents the vertical advection of radial flow; $VDR = K_v \cdot \partial^2 u'/\partial z^2$ represents the vertical diffusion of radial flow; $AAA = v_g/r \cdot \partial v'/\partial \lambda$ represents the azimuthal advection of azimuthal flow; $RAA = (\partial v_g/\partial r + v_g/r + f) \cdot u'$ represents the radial advection of azimuthal flow; $VAA = w' \partial v'/\partial z$ represents the vertical advection of azimuthal flow; $VDA = K_v \cdot \partial^2 v'/\partial z^2$ represents the vertical diffusion of azimuthal flow.

Figure 5 shows that the vertical diffusion (VDR and VDA) and radial advection (RAR and RAA) are predominant for near-surface layer (< 200 m). With the increase in height, the magnitude of vertical diffusion terms (VDR and VDA) decreases, and the magnitude of vertical advection terms (VAR and VAA) becomes larger, which takes second place above the height of 400 m. This indicates that the vertical advection
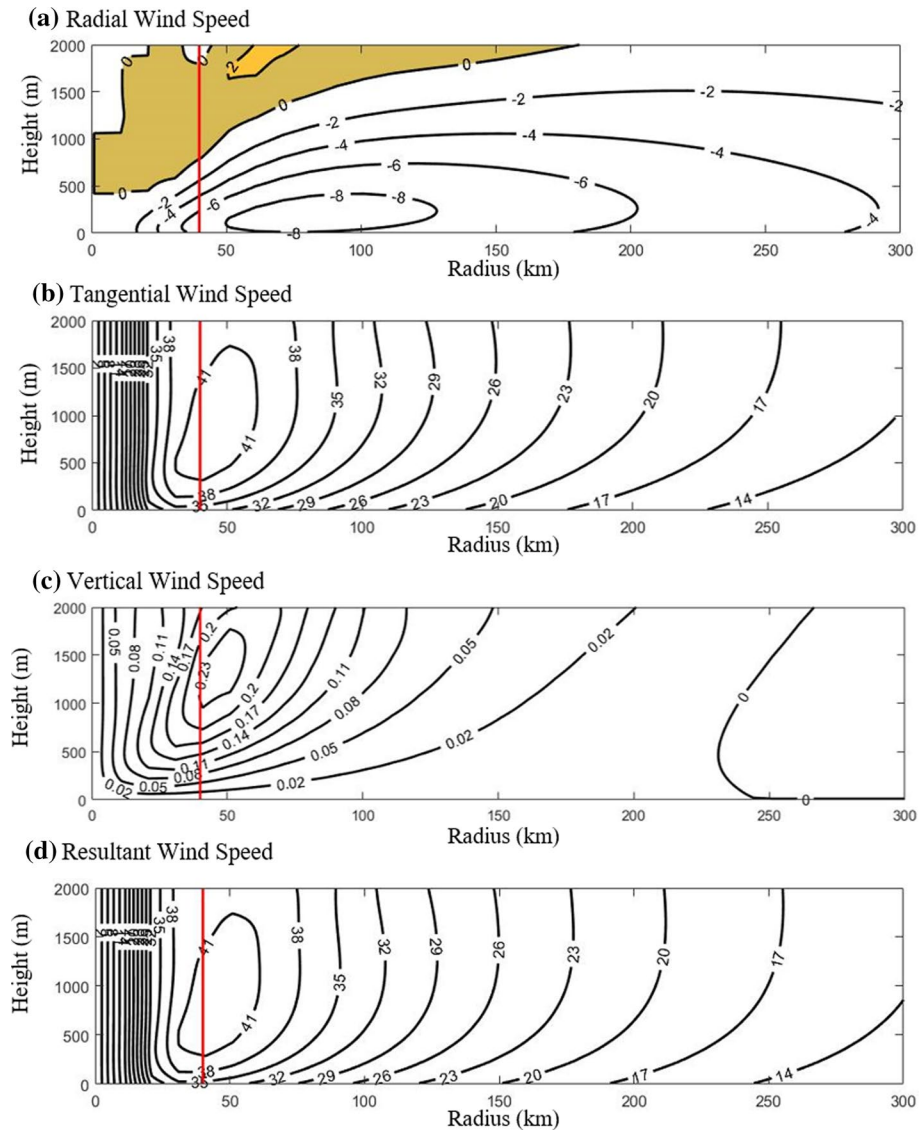
Fig. 4 Boundary layer solution for vertical cross sections of azimuthally averaged (**a**) radial wind speed, (**b**) tangential wind speed, (**c**) vertical wind speed and (**d**) resultant wind speed. The red lines are the radius to the maximum wind. Positive values are shaded in (**a**)

should not be ignored especially for wind field simulations above 400 m. In addition, all the advection and diffusion terms become nearly to zero at upper layer (> 1800 m), which is excepted because the wind speed above the TC boundary layer is nearly equal to the gradient wind and changes little with height.
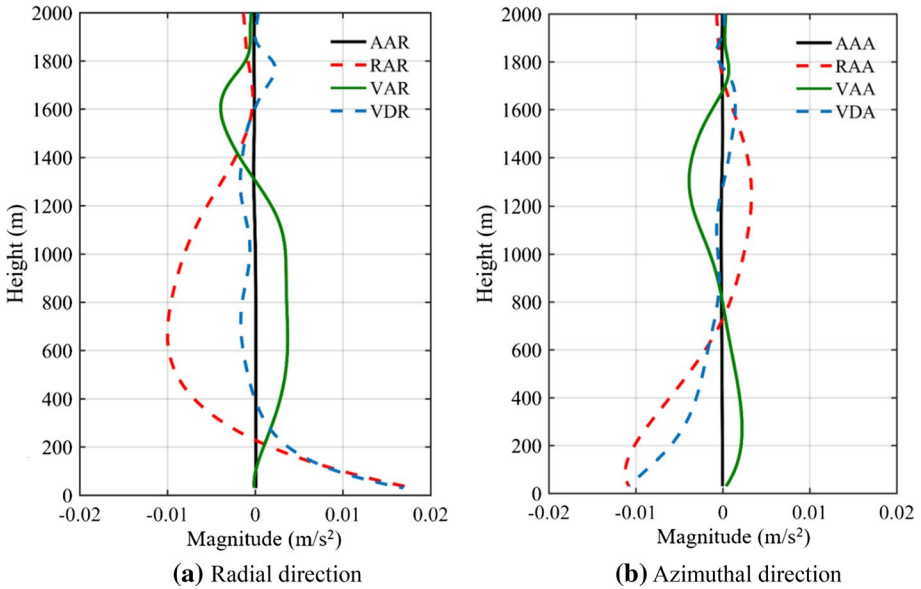
Fig. 5 Comparisons of azimuthally averaged advection and diffusion processes in Eqs. (5) and (6) at R_{max}. The TC case is same as in Fig. 3. $\text{AAR} = v_g/r \cdot \partial u'/\partial \lambda$, $\text{RAR} = -(2v_g/r + f) \cdot v'$, $\text{VAR} = w' \cdot \partial u'/\partial z$, $\text{VDR} = K_v \cdot \partial^2 u'/\partial z^2$, $\text{AAA} = v_g/r \cdot \partial v'/\partial \lambda$, $\text{RAA} = (\partial v_g/\partial r + v_g/r + f) \cdot u'$, $\text{VAA} = w' \cdot \partial v'/\partial z$, $\text{VDA} = K_v \cdot \partial^2 v'/\partial z^2$

3.3 Supergradient phenomenon

The supergradient phenomenon in TC boundary layer has been observed and studied by many scholars (Franklin et al. 2003; Giammanco et al. 2013; Kepert 2001; Kepert and Wang 2001; Vickery et al. 2009b). Franklin et al. (2003) investigated more than 215 profiles from TC eyewalls and more than 124 profiles from the outer vortex to statistically study the TC vertical wind profiles (wind speed profiles along height). In his observations, the wind speed reached its maximum at the height of 500 m and was about 20% larger than that at the height of 700 hPa for the eyewall. With over 1000 GPS dropsondes and 330 radar-derived velocity-azimuth display profiles, Giammanco et al. (2013) investigated the composite vertical wind profiles in different azimuthal sectors and their variations with radial distance. In addition, Kepert and Wang (2001) used a full numerical TC model to discuss the jet of TCs and found that the vertical advection was important in jet dynamics. The adequacy of the proposed model with vertical advection in capturing the supergradient feature is discussed in this section.

The normalized vertical wind profiles produced by the proposed model are shown in Fig. 6 together with those produced by M95 and K01. The jet heights (the heights of the maximum wind speed) and relative jet strengths ((the maximum wind speed—the gradient wind)/the gradient wind × 100%) are concluded in Table 2. As can be seen from Fig. 6 and Table 2, with the increase in TC intensity, the jet height becomes lower and the supergradient phenomenon becomes more pronounced, which is consistent with observations in Vickery et al. (2009b). In Table 2, the jet heights of the proposed model are higher than these of M95 and K01, and the relative jet strengths are nearly two times larger than these of the other two models. This indicates that the vertical advection can not only transport the turbulence to the upper layer but also strengthen the supergradient flow. Compared with stationary TC cases (Fig. 6a), the
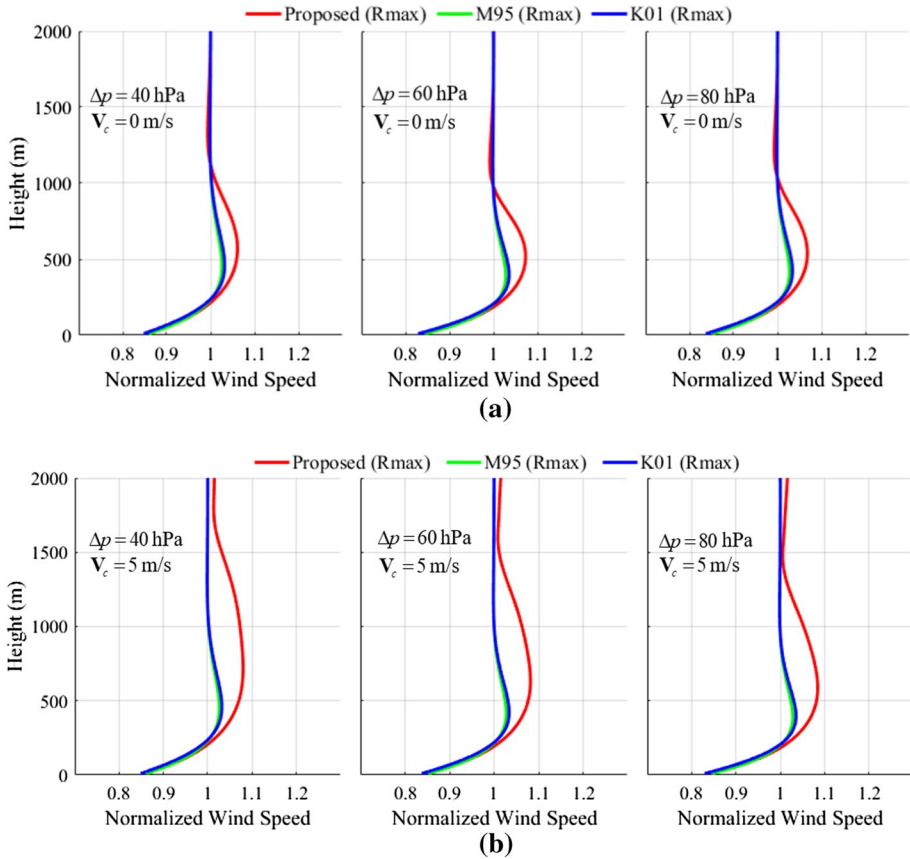
Fig. 6 Normalized vertical wind profiles at R_{max} of the proposed model, M95 and K01. The vertical wind profiles are azimuthally averaged and normalized to the gradient wind. Except for TC moving velocity ($\mathbf{V}_c$) and TC central pressure difference (Δp), the input parameters are same as in Fig. 3

movement of TC (Fig. 6b) enhances the supergradient phenomenon for the proposed model, but has less effects on M95 and K01.

4 Model validations

In this section, we will evaluate the proposed model by studying the horizontal wind fields, vertical wind profiles and near ground wind time series of several TC events. For horizontal wind fields, both the WRF simulations and H*Wind snapshots are used; for vertical wind profiles, the GPS dropsonde datasets are used. Comparisons with similar models such as the M95 and K01 are also made as necessary.

Table 2 Jet heights and relative jet strengths of the normalized vertical wind profiles in Fig. 6

V_c(m/s)	Δp(hPa)	Parameter	Proposed model	M95	K01
0	40	Jet Height (m)	570	460	450
		Relative Jet Strength (%)	6.1	3.2	2.6
	60	Jet Height (m)	540	420	420
		Relative Jet Strength (%)	6.8	3.4	2.7
	80	Jet Height (m)	520	400	390
		Relative Jet Strength (%)	7.3	3.6	2.8
5	40	Jet Height (m)	720	460	450
		Relative Jet Strength (%)	8.0	3.2	2.6
	60	Jet Height (m)	630	420	420
		Relative Jet Strength (%)	8.2	3.4	2.7
	80	Jet Height (m)	590	400	390
		Relative Jet Strength (%)	8.5	3.6	2.8

Jet height is the height of the maximum wind speed. Relative jet strength = (the maximum wind speed—the gradient wind)/the gradient wind × 100%

4.1 Horizontal wind fields

4.1.1 Comparison with WRF simulations

WRF is a mesoscale numerical weather prediction system designed for both atmospheric research and operational forecasting applications. It can produce simulations based on actual atmospheric conditions and has been widely used to study TC characteristics [e.g., Dodla et al. (2011), Li et al. (2013), Xue et al. (2017), Lu et al. (2018)]. In this study, WRF-ARW dynamical core, version 3.6, is used to simulate Typhoon Hagupit (2008), Hurricane Irene (2011) and Typhoon Lekima (2019) with horizontal grid spacing of 45, 15 and 5 km. The physical parameterization schemes used here are the Yonsei University planetary boundary layer scheme, Noah land surface scheme, Dudhia short-wave scheme, Rapid Radiative Transfer Model longwave scheme, Monin–Obukhov surface-layer scheme and WRF Single-Moment 6-class scheme. The initial and boundary conditions are interpolated from the NCEP Final Analysis data with one degree spatial resolution and six hourly temporal resolution. The simulation is started 24 h in advance. The wind fields simulated by WRF shown in Figs. 7 and 8 are calculated from the D03 simulation domain. (Horizontal grid spacing is 5 km)

The horizontal fields of the horizontal and vertical wind components at the height of 1000 m simulated by WRF are shown in Figs. 7 and 8, respectively, together with results by the proposed model, M95 and K01 for comparisons. R values in Figs. 7 and 8 are the Pearson correlation values between the WRF simulated results and the corresponding TC model simulated results. The input parameters (p_0, R_{max}, V_c, φ and lat) listed on the left side of each graph are extracted or inferred from the WRF simulation results. Specifically, R_{max} is inferred from the azimuthally averaged WRF simulated wind field at height of 1000 m; p_0 and lat are directly extracted from the WRF simulated surface pressure field; V_c and φ are estimated based on the TC center locations before and after the WRF simulated wind field shown in Fig. 7. B is calculated by Eq. 10. The vertical wind components of M95 and K01 are simulated using the
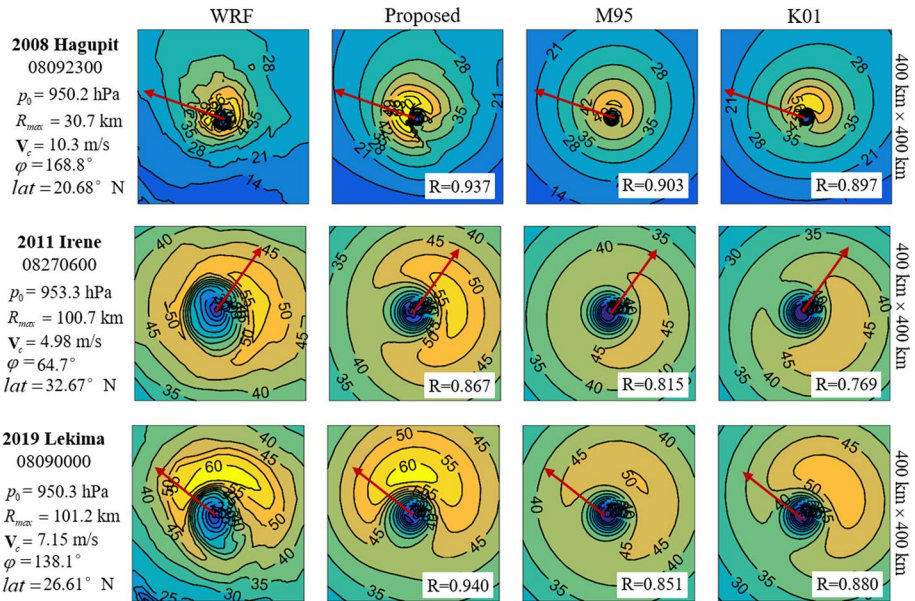
Fig. 7 Comparisons of horizontal wind component simulated by WRF, the proposed model, M95 and K01 at height of 1000 m. Value below the named hurricane refers to month, day, hour and minute. R is the Pearson correlation value between the WRF simulated horizontal wind component and the corresponding TC model simulated results. $z_0 = 0.0002$ m for TCs moving over the ocean. Red arrows are the TC moving directions

continuity equation (Eq. 7). Considering that the large vertical grid space in WRF may cause inaccurate calculations in the near-surface ground, wind fields at the height of 1000 m instead of 10 m are compared here.

For the horizontal wind components, as shown in Fig. 7, the maximum winds simulated by the proposed model locate on the front of TC's moving direction in Hagupit (2008), and on the right front in Irene (2011) and Lekima (2019), which resemble more like the WRF simulations than M95 and K01 do. This may be explained by the vertical advection which enhances the rotation of TC, but is neglected in M95 and K01. This phenomenon becomes more obvious for Hagupit (2008) that has a tighter structure. Comparing with M95 and K01, the Pearson correlation value (R) of the proposed model is the largest for these three TC events, which is 0.937 for Hagupit (2008), 0.867 for Irene (2011) and 0.940 for Lekima (2019). This shows that the proposed model is superior to the other two models in horizontal wind components simulations.

For the vertical wind components shown in Fig. 8, the horizontal field structures produced by the proposed model also look closer to the WRF simulations than the other two models do. The maximum vertical wind occurs at the same location as the horizontal wind. The magnitudes of vertical wind components given by the proposed model are larger than that of M95 and K01, but not as large as those given by WRF. The R values of the proposed model are more than two times larger than the values of M95 and K01 for vertical wind component simulations. This shows that considering the vertical advection can improve the model simulation ability of vertical wind component.
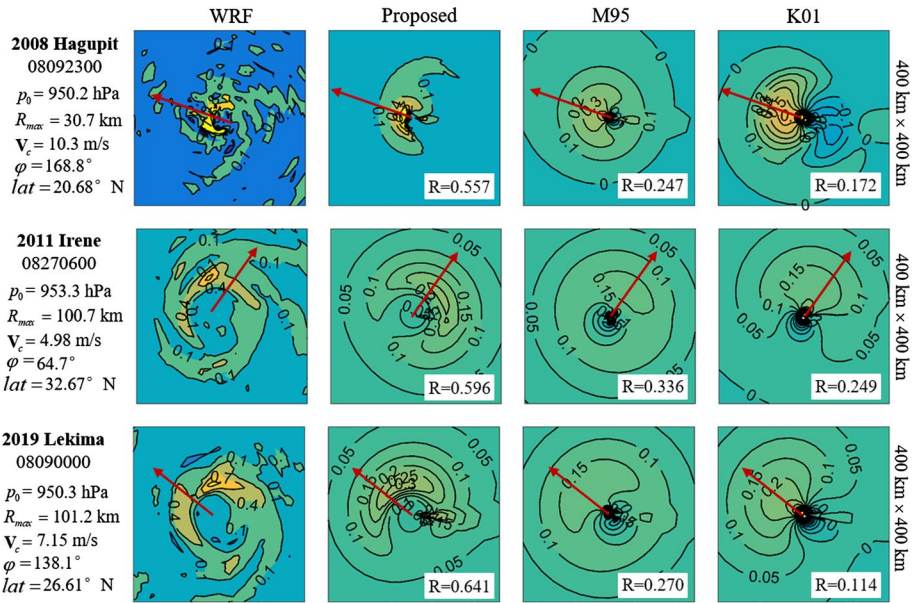
Fig. 8 Comparisons of vertical wind component simulated by WRF, the proposed model, M95 and K01 at height of 1000 m. Numbers below the named hurricanes refer to month, day, hour and minute. R is the Pearson correlation value between the WRF simulated vertical wind component and the corresponding TC model simulated results. $z_0 = 0.0002$ m for TCs moving over the ocean. Red arrows are the TC moving directions
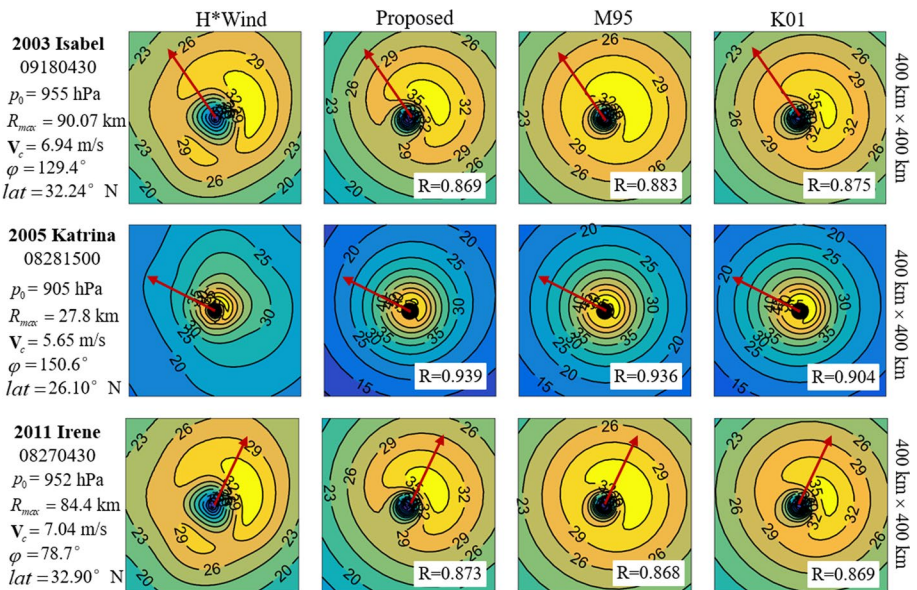

Fig. 9 Comparisons of H*Wind snapshots with the proposed model, M95 and K01 at height of 10 m; the numbers below the named hurricanes refer to month, day, hour and minute. R is the Pearson correlation value between the H*Wind snapshot and the corresponding simulated wind field. $z_0 = 0.0002$ m for TCs moving over the ocean. Red arrows are the TC moving directions

4.1.2 Comparison with H*Wind snapshots

H*Wind snapshots are considered to evaluate the performance of the proposed model. H*Wind was developed by the Hurricane Research Division of the National Oceanic and Atmospheric Administration (NOAA) and had transferred to HWind Scientific, a US private sector firm. Three TC snapshots obtained from http://www.rms.com/perils/hwind/legacy-archive/storms/ (no longer available from this address since April 2020) are shown in Fig. 9. TC moving velocity V_c, TC moving direction φ and TC center pressure p_0 in Fig. 9 are obtained from the National Hurricane Center's Hurricane Databases (HURDAT) Best Track Dataset (Landsea and Franklin 2013); R_{max} is derived from the azimuthally averaged corresponding H*Wind snapshots; B is calculated by Eq. (10). In order to compare with the simulated wind fields, the H*Wind snapshots are converted from 1-min sustained winds to 1-h averaging winds by using a conversion factor of 0.8 (the same as Fang et al. (2018)) and linearly interpolated into the same horizontal grid system as TC model used.

Horizontal wind fields at height of 10 m predicted by the proposed model, M95 and K01 are compared with the H*Wind snapshots shown in Fig. 9. The Pearson correlation values (R) between the H*Wind snapshots and corresponding simulated wind fields are also calculated. The comparison results show that the simulated wind fields of M95 and K01 match well with H*Wind snapshots at the same level as the proposed model does, and they all show a strong correlation with H*Wind snapshots. The minimum R value for Hurricane Isabel (2003) is 0.869, for Hurricane Katrina (2005) is 0.904 and for Hurricane Irene (2011) is 0.868. The small differences of R values and similar simulated wind fields among the proposed model, M95 and K01 indicates that the vertical advection may have little influence on the surface wind field simulations.

4.2 Vertical wind profiles

The development of GPS dropsonde allows the studies of the dynamic structures of TCs (Franklin et al. 2003). TC vertical wind profiles obtained from dropsonde datasets were firstly examined in a composite sense by Powell et al. (2003), in which five groups of wind profiles were defined according to the mean boundary layer (MBL) wind speed. Following the approach of Powell et al. (2003), Vickery et al. (2009b) investigated the mean vertical wind profiles for near and away from the radius to the maximum wind by using the Atlantic Oceanographic and Meteorological Laboratories Hurricane Research Division (AOML HRD) dropsonde datasets. Figure 10 shows six different groups of vertical wind profiles according to the MBL wind speed averaged over a height range from 10 to 500 m in Vickery et al. (2009b).

In the study, the proposed model, M95 and K01 are used to predict the mean vertical wind profiles. The input parameters for these three models are as follows. For R_{max} in the range of 10–30 km (Fig. 10a), R_{max} is set to the middle value of 20 km; in the range of 30–60 km (Fig. 10b), R_{max} is chosen to be 45 km; V_{max} (the maximum wind speed of v_g at R_{max}) is taken as the middle MBL wind speed bin value; V_c is set to be 0 m/s as the wind speed of GPS dropsonde datasets is assumed from a stationary and ergodic process (Powell et al. 2003; Vickery et al. 2009b); B is calculated by Eq. (10) with $f = 3.8 \times 10^{-5}$ s^{-1}; Δp ($= 1010 - p_0$) is estimated by Eqs. (8) and (11) using R_{max}, B and $V_{max} \approx v_g$ ($r = R_{max}$).
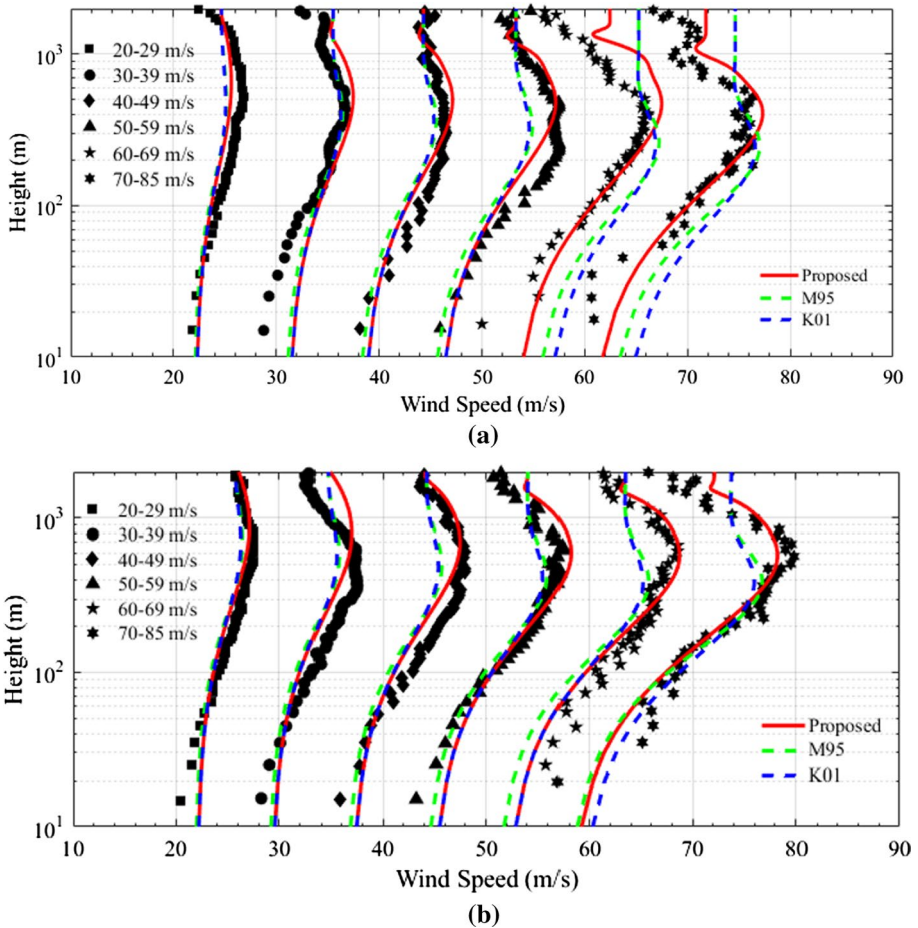
Fig. 10 Measured and simulated mean vertical wind profiles of TCs. **a** R_{max} ranges 10–30 km, **b** R_{max} ranges 30–60 km. Markers represent the composite GPS dropsonde data. 20–29, 30–39, 40–49, 50–59, 60–69 and 70–85 m/s are the six different MBL wind speed groups, which are extracted at different radii from TC center according to Vickery et al. (2009b) (his Fig. 2). $z_0 = 0.0002$ m for TCs moving over the ocean

Comparisons shown in Fig. 10 indicate that vertical wind profiles predicted by the proposed model closely approximate the profiles derived from the dropsonde data. For intense TCs, compared with the proposed model, the jet heights of M95 and K01 are lower, and the jet strengths are weaker, which is consistent with the studies in Sect. 3.3. Wind profiles near the ground surface do not follow a logarithmic law; instead, they have a nearly linear variation with height. This deficiency is due to the constant value of vertical eddy viscosity coefficient used in this study (Hong et al. 2019; Kepert 2012; Li et al. 2020).
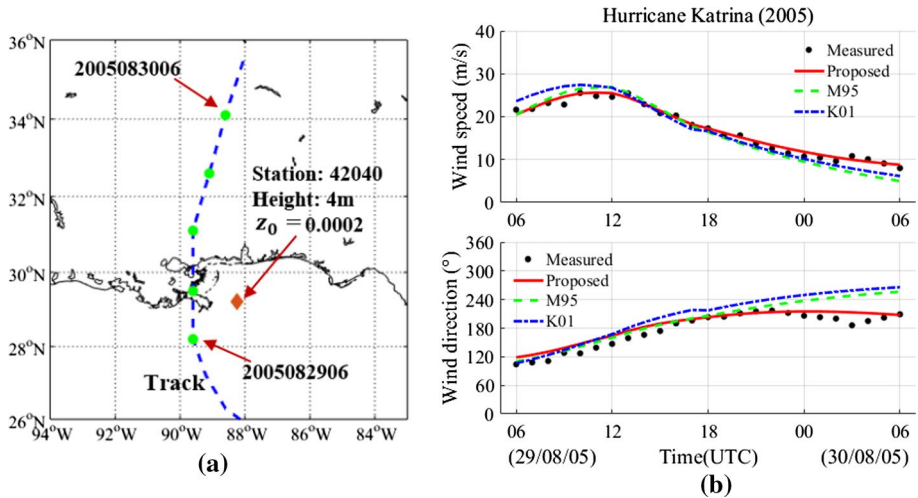
Fig. 11 Measured and simulated surface wind speeds and directions for Hurricane Katrina (2005)
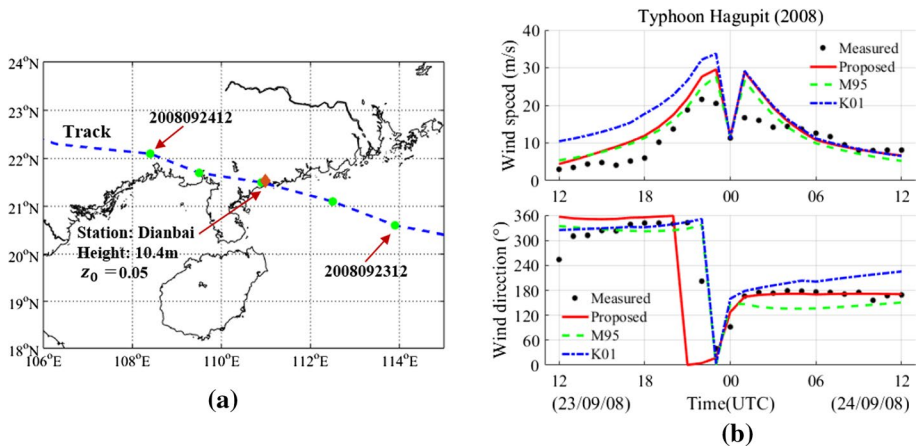

Fig. 12 Measured and simulated surface wind speeds and directions for Typhoon Hagupit (2008)

4.3 Near ground wind measurements of TCs

The proposed wind field model is validated by near ground surface measurements of three hurricanes (or typhoons), namely Katrina (2005), Hagupit (2008) and Irene (2011), which are the most destructive TCs attack the US coastal lines and the southeast China coastal regions. For hurricanes of the Gulf of Mexico, the historical Best Track Datasets from the National Hurricane Center's Hurricane Databases (HURDAT) (Landsea and Franklin 2013) are used, and the wind observations from the National Data Buoy Center are compared. For typhoon Hagupit (2008) moving on the Northwest Pacific Ocean, the historical Best Track Datasets are from the CMA Tropical Cyclone Data Center (Ming et al. 2014), and the surface wind observations from the Guangdong Meteorology Agency of China are compared. Specifically, the model input parameters of *lat* and p_0 are extracted from
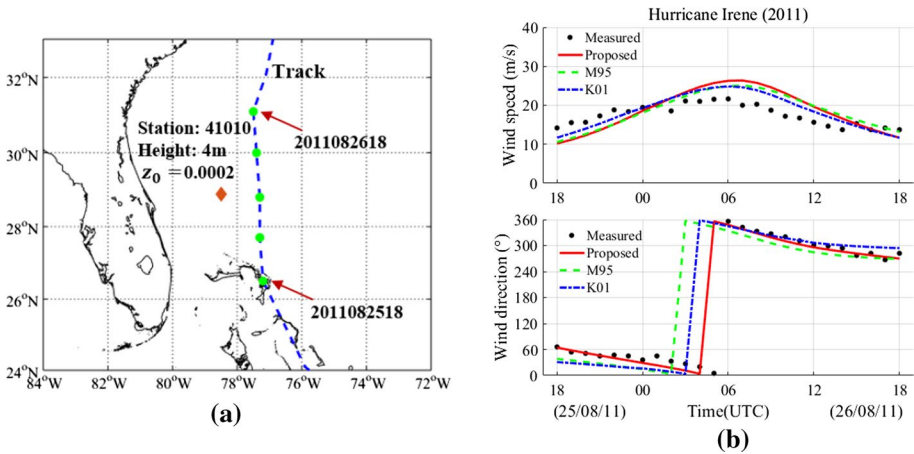
Fig. 13 Measured and simulated surface wind speeds and directions for Hurricane Irene (2011)

the historical Best Track Datasets and linearly interpolated to an hourly scale; $\mathbf{V}_c$ and φ are calculated from the before and after TC center locations; R_{max} and B are calculated from Eqs. (9) and (10). The TC tracks and meteorological station locations are shown in Figs. 11a, 12a and 13a.

Comparisons of the wind speeds and directions of the three hurricanes (or typhoons) are shown in Fig. 11b, 12b and 13b. Overall, the results demonstrate that wind velocities simulated by the three models match reasonably well with the measured data. For Hurricane Katrina (2005), both wind speeds and directions simulated by the proposed model match well with the measured data. For Typhoon Hagupit (2008), the simulated wind speeds of these three TC models (the proposed model, M95 and K01) are larger than the observed wind speeds. The simulated wind directions of the proposed model are match well with the observed data after 00:00:00 (UTC) on September 24, 2008. The deviations of wind speeds may be caused by the inaccurate surface roughness length used in Fig. 12, which varies with local topography and land cover types. For Hurricane Irene (2011), the simulated wind directions match better with the measured data than the simulated wind speeds do. These biases are acceptable considering the neglects of thermodynamic equations and simplifications of dynamic equations in TC wind field models.

5 Conclusions

A height-resolving model for TC wind field simulations is proposed in this paper, which considers the physical processes of horizontal advection, vertical advection and vertical diffusion. A semi-analytical solution is developed to solve the governing equations of this TC model.

Case study shows that the location of the maximum wind speed evaluated by the proposed model falls on the right quadrant at about 90° of TC moving direction near-surface ground and rotates toward the right front quadrant with increasing height. Due to the vertical advection, the proposed model predicts higher jet height and stronger jet strength than the Meng et al.

Table 3 Scales, magnitudes and units of variables in Eqs. (34) and (35)

Variable	u'	v'	w'	r	z	f	K_v	u_c	v_c	v_g
Scale	U	V	W	R	Z	f	K	U	V	V_g
Magnitude	10^0	10^0	10^{-1}	10^5	10^3	10^{-5}	10^1	10^0	10^0	10^1
unit	m/s	m/s	m/s	m	m	s^{-1}	m^2/s	m/s	m/s	m/s

Table 4 Scaling of the terms in Eq. (33)

$$\left(u_c + u'\right)\frac{\partial u'}{\partial r} + \frac{v_c + v'}{r}\frac{\partial u'}{\partial \lambda} + \frac{v_g}{r}\frac{\partial u'}{\partial \lambda} + w'\frac{\partial u'}{\partial z} - \frac{v_c v'}{r} - \frac{v'^2}{r} - \frac{2v'v_g}{r} = f \cdot v' +$$

$$\frac{UUVU}{R}\ \frac{V_g U}{R}\ \frac{WU}{Z}\ \frac{VV}{R}\ \frac{V^2}{R}\ \frac{2VV_g}{R}\ f\ V$$

$$10^{-5}\ 10^{-5}\ 10^{-4}\ 10^{-4}\ 10^{-5}\ 10^{-5}\ 2\cdot10^{-4}\ 10^{-5}$$

$$K_v\frac{1}{r}\frac{\partial}{\partial r}\left(r\frac{\partial u'}{\partial r}\right) + K_v\frac{1}{r^2}\frac{\partial^2 u'}{\partial \lambda^2} + K_v\frac{\partial^2 u'}{\partial z^2} - K_v\frac{u'}{r^2} - K_v\frac{2}{r^2}\frac{\partial(v_g + v')}{\partial \lambda}$$

$$K\frac{U}{R^2}\ K\frac{U^2}{R^2}\ K\frac{U^2}{Z^2}\ K\frac{U}{R^2}\ K\frac{2V_g}{R^2}$$

$$10^{-9}\ 10^{-9}\ 10^{-5}\ 10^{-9}\ 2\cdot10^{-8}$$

(1995) and Kepert (2001) models do, and with the increase in TC intensity, the predicted jet height becomes lower and the supergradient phenomenon becomes more pronounced.

With the WRF modeling of Typhoon Hagupit (2008), Hurricane Irene (2011) and Typhoon Lekima (2019) as the benchmark, the horizontal fields of the horizontal and vertical wind components at height of 1000 m simulated by the proposed model show greater resemblance than Meng et al. (1995) and Kepert (2001) models do. For the near ground surface winds, predictions of our model match well with the Hurricane Research Division's H*Wind snapshots at height of 10 m.

Vertical wind profiles predicted by the proposed model are consistent with those derived from the GPS dropsonde datasets except for the non-logarithmic profiles near the ground surface, which are mainly caused by the constant vertical eddy viscosity coefficient (K_v) used in this paper. The proposed model also reasonably simulates the ground observations of wind speeds and directions of three TC events.

In summary, by incorporating the vertical advection process, the proposed model improves on the wind field simulations over the previous models and reproduces more realistic three-dimensional wind structures in the boundary layer.

Appendix 1

In the cylindrical coordinate system, Eq. (3) can be expressed as

$$\left(u_c + u'\right)\frac{\partial u'}{\partial r} + \frac{v_c + v'}{r}\frac{\partial u'}{\partial \lambda} + \frac{v_g}{r}\frac{\partial u'}{\partial \lambda} + w'\frac{\partial u'}{\partial z} - \frac{v_c v' + v'^2 + 2v'v_g}{r} = f \cdot v' +$$

$$K_v\left[\frac{1}{r}\frac{\partial}{\partial r}\left(r\frac{\partial u'}{\partial r}\right) + \frac{1}{r^2}\frac{\partial^2 u'}{\partial \lambda^2} + \frac{\partial^2 u'}{\partial z^2} - \frac{1}{r^2}\left(u' + 2\frac{\partial(v_g + v')}{\partial \lambda}\right)\right] \tag{33}$$

Table 5 Scaling of the terms in Eq. (34)

$$(u_c + u')\frac{\partial v'}{\partial r} + \frac{v_c + v'}{r}\frac{\partial v'}{\partial \lambda} + \frac{v_g}{r}\frac{\partial v'}{\partial \lambda} + w'\frac{\partial v'}{\partial z} + \frac{u_c v'}{r} + \frac{u' v'}{r} + \frac{u' v_g}{r} + u'\frac{\partial v_g}{\partial r} = -f \cdot u' +$$

$\frac{UV}{R}$	$\frac{VV}{R}$	$\frac{V_g V}{R}$	$\frac{WU}{Z}$	$\frac{UV}{R}$	$\frac{UV}{R}$	$\frac{UV_g}{R}$	$\frac{UV_g}{R}$	$f\,U$
10^{-5}	10^{-5}	10^{-4}	10^{-4}	10^{-5}	10^{-5}	10^{-4}	10^{-4}	10^{-5}

$$K_v \frac{1}{r}\frac{\partial}{\partial r}\left(r\frac{\partial(v_g+v')}{\partial r}\right) + K_v \frac{1}{r^2}\frac{\partial^2(v_g+v')}{\partial \lambda^2} + K_v \frac{\partial^2(v_g+v')}{\partial z^2} - K_v\frac{(v_g+v')}{r^2} - K_v\frac{2}{r^2}\frac{\partial u'}{\partial \lambda}$$

$K\frac{V_g}{R^2}$	$K\frac{V^2}{R^2}$	$K\frac{V^2}{Z^2}$	$K\frac{V_g}{R^2}$	$K\frac{2U}{R^2}$
10^{-8}	10^{-9}	10^{-5}	10^{-8}	$2\cdot10^{-9}$

$$(u_c + u')\frac{\partial v'}{\partial r} + \frac{v_c + v'}{r}\frac{\partial v'}{\partial \lambda} + \frac{v_g}{r}\frac{\partial v'}{\partial \lambda} + w'\frac{\partial v'}{\partial z} + \frac{u_c v' + u' v' + u' u_g}{r} + u'\frac{\partial v_g}{\partial r} = -f \cdot u' +$$
$$K_v\left[\frac{1}{r}\frac{\partial}{\partial r}\left(r\frac{\partial(v_g+v')}{\partial r}\right) + \frac{1}{r^2}\frac{\partial^2(v_g+v')}{\partial \lambda^2} + \frac{\partial^2(v_g+v')}{\partial z^2} - \frac{1}{r^2}\left((v_g+v') - 2\frac{\partial u'}{\partial \lambda}\right)\right]$$

$$\tag{34}$$

in which, u', v' and w' are the radial, tangential and vertical friction caused wind components, respectively; r, λ and z are the radial, azimuthal and vertical variables, respectively; u_c and v_c are the radial and tangential components of $\mathbf{V}_c$. It should be noted that the radial component of the gradient wind (u_g) is assumed to be zero. Scale analysis is used here to simplify Eqs. (33) and (34), and the variable magnitudes of a tropical cyclone are listed in Table 3.

The scaling terms and magnitudes of Eqs. (33) and (34) are listed in Tables 4 and 5. For simplicity, we only consider the terms whose magnitudes larger than 10^{-4}. The Coriolis terms and vertical diffusion terms are retained for their importance in TC wind field simulations. Then, we have

$$\frac{v_g}{r}\frac{\partial u'}{\partial \lambda} - \left(\frac{2v_g}{r} + f\right)v' + w'\frac{\partial u'}{\partial z} = K_v\frac{\partial^2 u'}{\partial z^2}$$

$$\tag{35}$$

$$\frac{v_g}{r}\frac{\partial v'}{\partial \lambda} + \left(\frac{\partial v_g}{\partial r} + \frac{v_g}{r} + f\right)u' + w'\frac{\partial v'}{\partial z} = K_v\frac{\partial^2 v'}{\partial z^2}$$

$$\tag{36}$$

Appendix 2

Here, we assume the friction wind components u' and v' to be zero as $z \to +\infty$. The p_k in Eq. (26) can be solved as

$$p_k = \delta - \sqrt{2i\sqrt{\alpha\beta} + 2ik\gamma + \delta^2}$$

$$\tag{37}$$

Let

$$t_k = \sqrt{2i\sqrt{\alpha\beta} + 2ik\gamma + \delta^2} = a + bi$$

$$\tag{38}$$

where $a = \mathrm{Re}(t_k)$, $b = \mathrm{Im}(t_k)$. For $\sqrt{\alpha\beta} + k\gamma \geq 0$, $p_k = \delta - [|a| + |b|i]$; for $\sqrt{\alpha\beta} + k\gamma < 0$, $p'_k = \delta - [|a| - |b|i]$.

After some manipulations of terms in Eqs. (27) and (28), for $\sqrt{\alpha\beta} + k\gamma \geq 0$ and $|k| \leq 1$, we have the following equations.

For $k = 0$,

$$-\sqrt{\frac{\alpha}{\beta}}A_0 p_0 - \sqrt{\frac{\alpha}{\beta}}A_0^* p_0^* + \sqrt{\frac{\alpha}{\beta}}\frac{A_0 C_d v_g}{K_v} + \sqrt{\frac{\alpha}{\beta}}\frac{A_0^* C_d v_g}{K_v} = 0 \tag{39}$$

$$A_0 p_0 - A_0^* p_0^* - \frac{2A_0 C_d v_g}{K_v} + \frac{2A_0^* C_d v_g}{K_v} - \frac{2iC_d v_g^2}{K_v} = 0 \tag{40}$$

For $k = 1$,

$$-\sqrt{\frac{\alpha}{\beta}}A_1 p_1 - \sqrt{\frac{\alpha}{\beta}}A_{-1}^* p_{-1}^* + \sqrt{\frac{\alpha}{\beta}}\frac{A_1 C_d v_g}{K_v} + \sqrt{\frac{\alpha}{\beta}}\frac{A_{-1}^* C_d v_g}{K_v} + \frac{\mathbf{V}_c C_d v_g}{K_v} = 0 \tag{41}$$

$$A_1 p_1 - A_{-1}^* p_{-1}^* - \frac{2A_1 C_d v_g}{K_v} + \frac{2A_{-1}^* C_d v_g}{K_v} + \frac{2V_c C_d v_g}{K_v} = 0 \tag{42}$$

For $k = -1$,

$$-\sqrt{\frac{\alpha}{\beta}}A_{-1} p_{-1} - \sqrt{\frac{\alpha}{\beta}}A_1^* p_1^* + \sqrt{\frac{\alpha}{\beta}}\frac{A_{-1} C_d v_g}{K_v} + \sqrt{\frac{\alpha}{\beta}}\frac{A_1^* C_d v_g}{K_v} + \frac{\mathbf{V}_c C_d v_g}{K_v} = 0 \tag{43}$$

$$A_{-1} p_{-1} - A_1^* p_1^* - \frac{2A_{-1} C_d v_g}{K_v} + \frac{2A_1^* C_d v_g}{K_v} - \frac{2V_c C_d v_g}{K_v} = 0 \tag{44}$$

In the above equations, $*$ indicates a complex conjugate. A_0, A_1 and A_{-1} can be derived from Eqs. (39) and (40), (41) and (42), (43) and (44), respectively, and we have

$$A_0 = -\frac{2iC_d v_g^2(-K_v p_0^* + C_d v_g)}{2K_v^2 p_0 p_0^* - 3K_v C_d p_0 v_g - 3K_v C_d p_0^* v_g + 4C_d^2 v_g^2} \tag{45}$$

$$A_1 = \frac{\mathbf{V}_c C_d v_g \left(K_v p_{-1}^* - 2K_v \sqrt{\frac{\alpha}{\beta}} p_{-1}^* - 2C_d v_g + 2\sqrt{\frac{\alpha}{\beta}} C_d v_g \right)}{\sqrt{\frac{\alpha}{\beta}}\left(2K_v^2 p_1 p_{-1}^* - 3K_v C_d p_1 v_g - 3K_v C_d p_{-1}^* v_g + 4C_d^2 v_g^2 \right)} \tag{46}$$

$$A_{-1} = \frac{\mathbf{V}_c C_d v_g \left(K_v p_1^* + 2K_v \sqrt{\frac{\alpha}{\beta}} p_1^* - 2C_d v_g - 2\sqrt{\frac{\alpha}{\beta}} C_d v_g \right)}{\sqrt{\frac{\alpha}{\beta}}\left(2K_v^2 p_{-1} p_1^* - 3K_v C_d p_{-1} v_g - 3K_v C_d p_1^* v_g + 4C_d^2 v_g^2 \right)} \tag{47}$$

For $\sqrt{\alpha\beta} + k\gamma < 0$, one can easily have

$$A'_1 = \frac{V_c C_d v_g \left(K_v p^{*\prime}_{-1} - 2K_v \sqrt{\frac{\alpha}{\beta}} p^{*\prime}_{-1} - 2C_d v_g + 2\sqrt{\frac{\alpha}{\beta}} C_d v_g \right)}{\sqrt{\frac{\alpha}{\beta}} \left(2K_v^2 p_1 p^{*\prime}_{-1} - 3K_v C_d p_1 v_g - 3K_v C_d p^{*\prime}_{-1} v_g + 4C_d^2 v_g^2 \right)} \tag{48}$$

$$A'_{-1} = \frac{\mathbf{V}_c C_d v_g \left(K_v p^{*}_1 + 2K_v \sqrt{\frac{\alpha}{\beta}} p^{*}_1 - 2C_d v_g - 2\sqrt{\frac{\alpha}{\beta}} C_d v_g \right)}{\sqrt{\frac{\alpha}{\beta}} \left(2K_v^2 p'_{-1} p^{*}_1 - 3K_v C_d p'_{-1} v_g - 3K_v C_d p^{*}_1 v_g + 4C_d^2 v_g^2 \right)} \tag{49}$$

Finally, the friction caused wind components (u', v') in the TC boundary layer are, for $\sqrt{\alpha\beta} + k\gamma \geq 0$,

$$u'(r, \lambda, z) = \sqrt{\frac{\alpha}{\beta}} \cdot \mathrm{Re}\left[A_{-1} \exp(p_{-1} \cdot z - i\lambda) + A_0 \exp(p_0 \cdot z) + A_1 \exp(p_1 \cdot z + i\lambda) \right] \tag{50}$$

$$v'(r, \lambda, z) = \mathrm{Im}\left[A_{-1} \exp(p_{-1} \cdot z - i\lambda) + A_0 \exp(p_0 \cdot z) + A_1 \exp(p_1 \cdot z + i\lambda) \right] \tag{51}$$

for $\sqrt{\alpha\beta} + k\gamma < 0$,

$$u'(r, \lambda, z) = \sqrt{\frac{\alpha}{\beta}} \cdot \mathrm{Re}\left[A'_{-1} \exp(p'_{-1} \cdot z - i\lambda) + A'_0 \exp(p'_0 \cdot z) + A'_1 \exp(p'_1 \cdot z + i\lambda) \right] \tag{52}$$

$$v'(r, \lambda, z) = \mathrm{Im}\left[A'_{-1} \exp(p'_{-1} \cdot z - i\lambda) + A'_0 \exp(p'_0 \cdot z) + A'_1 \exp(p'_1 \cdot z + i\lambda) \right] \tag{53}$$

Compliance with ethical standards

Conflicts of interest The authors declare that they have no known competing financial interests or personal relationships that could have appeared to influence the work reported in this paper.

References

BattsASCE MEAM, Russell LR, Simiu E (1980) Hurricane wind speeds in the United States. J Struct Div 106:2001–2016

Bell MM, Montgomery MT (2008) Observed structure, evolution, and potential intensity of category 5 hurricane Isabel (2003) from 12 to 14 September. Mon Weather Rev 136:2023–2046

Chen Y, Duan Z (2018) A statistical dynamics track model of tropical cyclones for assessing typhoon wind hazard in the coast of southeast China. J Wind Eng Ind Aerodyn 172:325–340

Chow SH (1971) A study of the wind field in the planetary boundary layer of a moving tropical cyclone. New York University, New York

Dodla VB, Desamsetti S, Yerramilli A (2011) A comparison of HWRF, ARW and NMM models in Hurricane Katrina (2005) simulation. Int J Environ Res Public Health 8:2447–2469

Fang G, Zhao L, Cao S, Ge Y, Pang W (2018) A novel analytical model for wind field simulation under typhoon boundary layer considering multi-field correlation and height-dependency. J Wind Eng Ind Aerodyn 175:77–89

Franklin JL, Black ML, Valde K (2003) GPS Dropwindsonde wind profiles in hurricanes and their operational implications. Weather Forecast 18:32–44

Giammanco IM, Schroeder JL, Powell MD (2013) GPS Dropwindsonde and WSR-88D observations of tropical cyclone vertical wind profiles and their characteristics. Weather Forecast 28:77–99

Holland GJ (1980) An analytic model of the wind and pressure profiles in hurricanes. Mon Weather Rev 108:1212–1218

Holton JR (2007) An introduction to dynamic meteorology, vol 88. Elsevier Academic Press, Boston

Hong HP, Li SH, Duan ZD (2016) Typhoon wind hazard estimation and mapping for coastal region in Mainland China. Natural Hazards Rev 17:1–13

Hong X, Hong HP, Li J (2019) Solution and validation of a three dimensional tropical cyclone boundary layer wind field model. J Wind Eng Ind Aerodyn 193:103973

Kepert J (2001) The dynamics of boundary layer jets within the tropical cyclone core. Part i: linear theory. J Atmosph Sci 58:2469–2484

Kepert J, Wang Y (2001) The dynamics of boundary layer jets within the tropical cyclone core. Part II: nonlinear enhancement. J Atmosph Sci 58:2485–2501

Kepert JD (2010a) Slab- and height-resolving models of the tropical cyclone boundary layer. Part I: comparing the simulations. Quarterly J Royal Meteorol Soc 136:1686–1699

Kepert JD (2010b) Slab- and height-resolving models of the tropical cyclone boundary layer. Part II: Why the simulations differ. Quarterly J Royal Meteorol Soc 136:1700–1711

Kepert JD (2012) Choosing a boundary layer parameterization for tropical cyclone modeling. Mon Weather Rev 140:1427–1445

Landsea CW, Franklin JL (2013) Atlantic Hurricane database uncertainty and presentation of a new database format. Mon Weather Rev 141:3576–3592

Langousis A, Veneziano D (2009) Theoretical model of rainfall in tropical cyclones for the assessment of long-term risk. J Geophys Res 114:D02106

Langousis A, Veneziano D, Chen S (2009) Boundary layer model for moving tropical cyclones. In: Elsner JB, Jagger TH (eds) Hurricanes and climate change. Springer, Boston, pp 265–286

Li J, Gang W, Lin W, He Q, Feng Y, Mao JJAR (2013) Cloud-scale simulation study of Typhoon Hagupit (2008) Part I: Microphysical processes of the inner core and three-dimensional structure of the latent heat budget. Atmos Res 120–121:170–180

Li SH, Hong HP (2015) Observations on a hurricane wind hazard model used to map extreme hurricane wind speed. J Struct Eng 141:1–12

Li W, Hu Z, Pei Z, Li S, Chan PW (2020) A discussion on influences of turbulent diffusivity and surface drag parameterizations using a linear model of the tropical cyclone boundary layer wind field. Atmos Res 237:104847

Lu P, Lin N, Emanuel K, Chavas D, Smith J (2018) Assessing hurricane rainfall mechanisms using a physics-based model: hurricanes Isabel (2003) and Irene (2011). J Atmos Sci 75:2337–2358

Meng Y, Masahiro M, Kazuki H (1995) An analytical model for simulation of the wind field in a typhoon boundary layer. J Wind Eng Ind Aerodyn 56:291–310

Ming Y et al (2014) An overview of the china meteorological administration tropical cyclone database. J Atmosph Oceanic Technol 31:287–301

Powell M et al (2005) State of Florida hurricane loss projection model: atmospheric science component. J Wind Eng Ind Aerodyn 93:651–674

Powell MD, Vickery PJ, Reinhold TA (2003) Reduced drag coefficient for high wind speeds in tropical cyclones. Nature 422:279–283

Schwendike J, Kepert JD (2008) The Boundary layer winds in hurricanes Danielle (1998) and Isabel (2003). Mon Weather Rev 136:3168–3192

Shapiro LJ (1983) The asymmetric boundary layer flow under a translating Hurricane. J Atmosph Sci 40:1984–1998

Snaiki R, Wu T (2017a) A linear height-resolving wind field model for tropical cyclone boundary layer. J Wind Eng Ind Aerodyn 171:248–260

Snaiki R, Wu T (2017b) Modeling tropical cyclone boundary layer: height-resolving pressure and wind fields. J Wind Eng Ind Aerodyn 170:18–27

Sparks PR, Huang Z (2001) Gust factors and surface-to-gradient wind-speed ratios in tropical cyclones. J Wind Eng Ind Aerodyn 89:1047–1058

Thompson EF, Cardone VJ (1996) Practical modeling of hurricane surface wind fields. J Waterway Port Coastal Ocean Eng 122:195–205

Vickery PJ, Masters FJ, Powell MD, Wadhera D (2009a) Hurricane hazard modeling: the past, present, and future. J Wind Eng Ind Aerodyn 97:392–405

Vickery PJ, Wadhera D (2008) Statistical models of Holland pressure profile parameter and radius to maximum winds of hurricanes from flight-level pressure and h*wind data. J Appl Meteorol Climatol 47:2497–2517

Vickery PJ, Wadhera D, Powell MD, Chen Y (2009b) A Hurricane boundary layer and wind field model for use in engineering applications. J Appl Meteorol Climatol 48:381–405

Vickery PJ, Wadhera D, Twisdale LA, Lavelle FM (2009c) U.S. Hurricane wind speed risk and uncertainty. J Struct Eng 135:301–320

Vogl S, Smith RK (2009) Limitations of a linear model for the hurricane boundary layer. Quarterly J Royal Meteorol Soc 135:839–850

Xiao YF, Duan ZD, Xiao YQ, Ou JP, Chang L, Li QS (2011) Typhoon wind hazard analysis for southeast China coastal regions. Struct Saf 33:286–295

Xue L, Li Y, Song L, Chen W, Wang B (2017) A WRF-based engineering wind field model for tropical cyclones and its applications. Nat Hazards 87:1735–1750